Progress In Electromagnetics Research B, Vol. 60, 125–139, 2014

New High-Rate UWB Scheme for WBAN-Based Healthcare Systems

Zakaria Mohammadi[1, *], Rachid Saadane[2], and Driss Aboutajdine[1]

Abstract—Given the emphasis on increasing wireless network usage for healthcare application, e.g., Wireless Body Area Network (WBAN), the need for high-rate physical layer has become a genuine concern from research and industrial community. The use of the Ultra-Wideband (UWB) is looking especially bright for such systems given its lower energy consumption and performances towards frequency-selective channels. However, the Multi-Band-OFDM-based UWB technique has some inherent limitations as loss in spectral efficiency due to the use of Cyclic-Prefix (CP). In this paper, a new physical layer scheme for high-rate wireless body area networks based on MB-OFDM with Offset Quadrature Amplitude Modulation (OQAM) modulation is presented. The proposed MB-OFDM/OQAM can achieve high spectral and power efficiency than conventional MB-OFDM system. Moreover, the use of the CP Interval in the conventional MBOFDM removes efficiently the Inter-Symbols Interferences (ISI) but remains ineffective towards the Inter-Carriers Interferences (ICI) caused by the channel frequency offset (FO). The performances evaluation of the proposed technique will be carried-out in realistic UWB-WBANs channels with various scenarios, which will be also presented and studied herein.

1. INTRODUCTION

The Wireless Body Area Networks [1] have encountered continuous developments and improvements during recent years. In such systems, as well as being surgically implanted, on/near the human body, the wearable sensors are used to monitor important vital signs: Electroencephalographic (EEG), Electrocardiographic (ECG), Electromyographies (EMG), ... The wireless aspect and the wide variety of the wearable sensors provide new functionalities for improving the performance of the health sector and life quality while maintaining the patients mobility and some independence vis-a-vis the medical staff. The provided informations thereafter can be sent to a remote clinic so that there can be interpreted by a specialist for a medical check-up, or in anticipation of a possible anomaly. As illustrated in Fig. 1, the real-time vital signs monitoring systems [2] consist of one or many sensors attached to body, while the coordinator is the appropriate equipment responsible for making important decisions, managing the resources and delivering measured data both within and beyond the local network [3]. This device is commonly referred to as Personal Base Station (PBS).

However, the WBANs principal concerns are associated with miniaturisation, energy consumption and sensors lifetime. Traditional narrow-band protocols, such as Medical Implant Communications Service MICS [4], Zigbee, ISM or Bluetooth [5] are hampered by high power consumption and low transmission data-rate. On the other hand, the Ultra wide-band (UWB) technology has been approved for use in WBANs [6] because of their extremely wide frequency band under low power consumption (EIRP$^{\dagger} < -41.3\,$dBm). This way, the UWB interference with existing wireless devices can be minimized. A further reason for using UWB is the limited impact of UWB devices on human organs.

The energy consumption presents a major challenge for WBANs, since patients have little motivation to adopt such solutions if the sensors battery should be recharged frequently or even strictly

Received 2 May 2014, Accepted 19 June 2014, Scheduled 24 June 2014

* Corresponding author: Zakaria Mohammadi (z.mohammadi@fsr.um5a.ma).

[1] GSCM-LRIT Laboratry Associate Unit to CNRST, Mohammed V-Agdal University, Rabat, Morocco. [2] LETI Laboratory, Hassania des Travaux Publiques, KM.7 Route d'EL Jadida, Casablanca, BP 8108, Morocco.

† Equivalent Isotropically Radiated Power

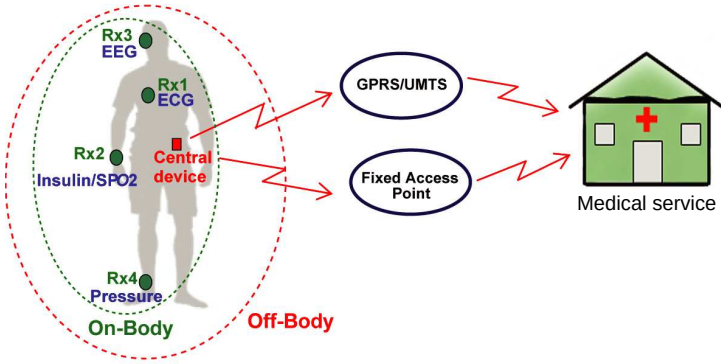

Figure 1. On-body and off-body scenarios for WBANs.

changed. Furthermore, reduced energy consumption is synonymous of a much smaller form factor, which deals with the problem of sensors miniaturization for the WBANs. However, some specific WBANs applications reflect the greatest need for sufficient throughput to transmit vital information to a distant destination. As an example, we report a high-rate wireless transmission system named HermesD [7], used to record and transmit neural activity from implanted electrode arrays, and supports the transmission of 32 simultaneous broadband data channels including synchronization and error detection mechanisms. Sometimes, even only one sensor can record more than one vital signs. For example, the AMON device [8] serves to acquire different informations from patient wrist: blood pressure (BP), electrocardiogram (ECG), blood oxygen saturation monitoring, galvanic skin response. The goal of this paper is to present a new uwb-based transmission scheme for WBANs, which beside providing high transmission rate, it gives better performances through multipath channels, as is the case for UWB-WBAN channels. However, it is worth looking in more detail on the specificity of the UWB-WBAN channel characteristics, essentially because of presence of the human body on the propagation environment. As complex as the shape and the density of human body is, it represents a hostile environment for the propagation of electrical waves, all the more so as the human tissues have different dielectric properties. The rest of paper is organized as follows: Section 2 reviews the UWB sounding campaign for measuring the UWB-WBANs channel response. The investigation of the characteristics of UWB channel in presence of human body are also provided. The next section discusses and presents an overview of the proposed UWB-based scheme. Finally, the performances of the UWB-based MBOFDM/OQAM performances are evaluated.

2. UWB-WBAN CHANNEL SURVEY

In order to examine the channel variations caused by the presence of a body in the propagation area, two types of experimentations were undertaken. The first one was performed in the anechoic chamber, to consider just the body placed therein, while the second were made in the Body-Centric Wireless Sensor laboratory of the London Queen-Mary university, to also include the effects of the walls, furniture and objects that may be present in the indoor environment. More detailed information can be viewed in [9]. The Channel Transfer functions CTF were acquired within the 3–10 GHz band (Temporal resolution $\Delta t = 0.14$ ns), at a sampling rate of 1601 bins ($\Delta f = 4.37$ MHz), which corresponds to a maximal excess delay of 228.8 ns. The Tapered-Slot antennas were connected to the Vector Network Analyzer (Agilent N5230C PNA-X) with low losses coaxial cable of 5 m. Fig. 2 illustrates different configurations for different measurements, while the transmitter Tx is fixed on the waist.

Then, the measured channel data are analyzed to extract Path-Loss (PL) and shadowing characteristics for different Rx positions. The PL value, which describes the attenuation of the received power, can be seen as the large-scale fading of the channel. This value was calculated for different Rx positions. Fig. 3 shows the distributions of the calculated PL value for different configurations as well as the corresponding Lognormal fit. The position of the Rx antenna impacts the PL value. Moreover, the calculated PL for the laboratory is greater than the anechoic value. This is due the new discovered path

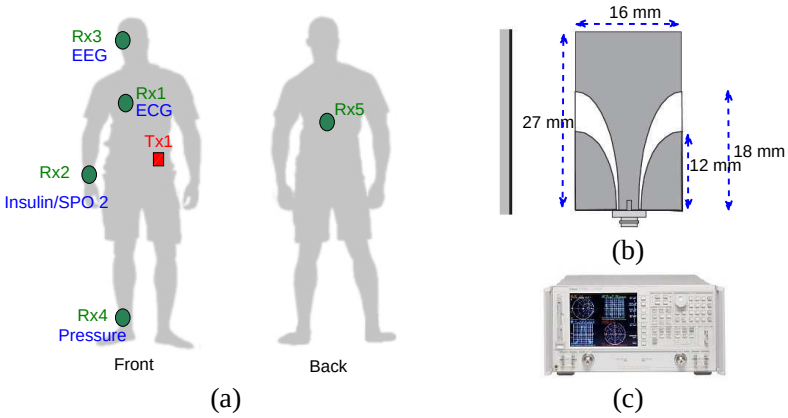

Figure 2. Configurations of the (a) Rx antenna positions where Tx-on-waist, (b) the TSA, and (c) the VNA used in the sounding compaign.

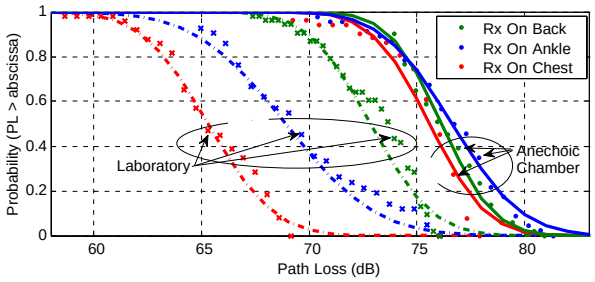

Figure 3. Cumulative distribution of measured PL-value for different Rx positions, in anechoic and laboratory rooms, Tx-on-waist.

caused by the introduction of walls and furniture in the laboratory chamber. It is worth noting that for anechoic chamber, the PL values for the three configurations do not show a significant difference, whereas for the laboratory room the disparity between calculated PL values is growing larger. It is noticeable that for Rx-On-Back, the PL value is higher than other positions since the Line Of Sight (LOS) is obstructed. As well, this value is higher for Rx-On-Ankle than for Rx-On-Chest due to different distances between the antennas.

In time domain, the impulse response (IR) is obtained through Fourier transform of the estimated CTF. Fig. 4 illustrates the estimated IR for different Rx positions, both in anechoic and laboratory chamber. As aforementioned, the introduction of the walls and furniture in the propagation area will contribute with new multi-path components MPCs, but would not necessarily increase the correspondant amplitude for different excess delays. As can be seen from Fig. 4, the constructive and destructive superpositions of the waves transmitted across the body and those transformed by the indoor obstacles will attenuate or amplify the channel response depending on the phase of arrival MPCs. For example, two paths arriving with some phase cause the amplification of the received MPC amplitude, while the phase opposition induces an attenuation of MPC amplitude. Moreover, Fig. 5 shows the inverse cumulative distribution of the Root Mean Square Delay Spread τ_{RMS} for different Rx positions (Tx fixed on Waist) and also the corresponding Lognormal fitting with a threshold of -25 dB. We can observe that measurements performed in the laboratory room for different Rx positions often give rise to higher τ_{RMS} values. In other words, the higher is the number of Multipath components (obstacles), the higher is the delay spread of the propagation channel.

More generally, the configuration of the human body is not static. The Rx antenna position will therefore be considered moving beside Tx antenna position. Thereby, three wrist motion will be considered herein as depicted in Fig. 6. The evolution of the UWB-WBAN Channel Impulse Response (CIR), for different sweeps, when the arm moves in the Down-Up direction is plotted in Fig. 7. As

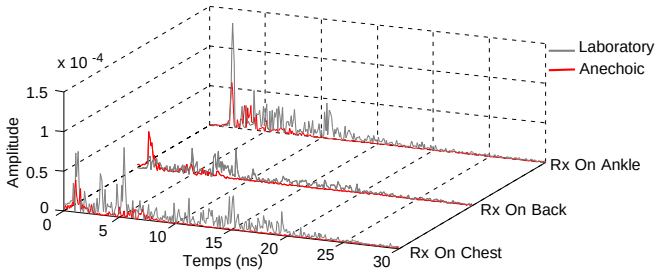

Figure 4. Plot of the impulse response for different positions of Rx for both Laboratory and anechoic chamber, Tx-on-waist.

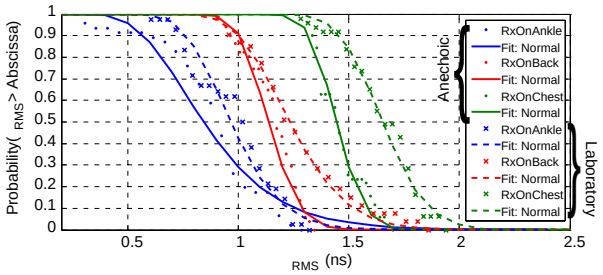

Figure 5. Plot of RMS delay distribution different Rx positions, in both anechoic and laboratory, Tx-on-waist.

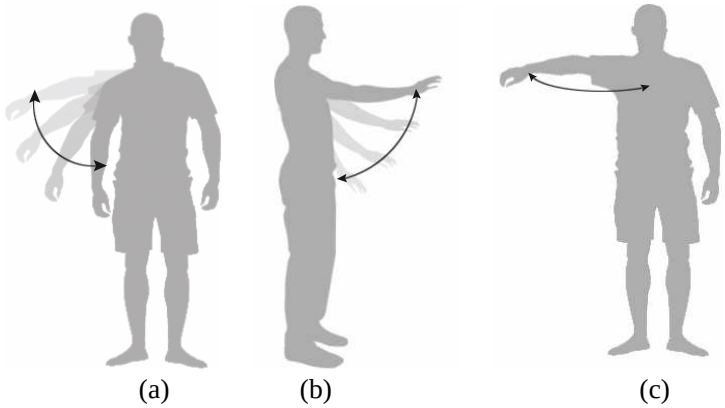

Figure 6. Considered wrist movements, where Rx fixed on waist and Tx on wrist: (a) side-up-down, (b) up-down, and (c) circular-front.

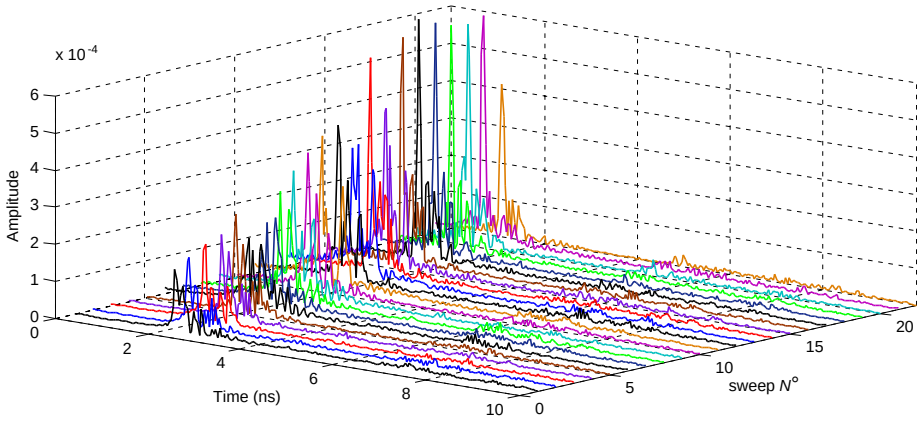

Figure 7. Evolution of the channel impulse response for different down-up motion sweeps, Rx-on-wrist and Tx-on-waist.

can be depicted, the first sweeps, which appear to correspond to the case where the Line Of Sight (LOS) between Rx and Tx antennas is obstructed by the human body, have the lowest amplitudes. Once the LOS between them becomes visible, this will lead to an amplification of the first arriving ray amplitude. The channel delay spread, characterized by the Root Mean Square Delay Spread τ_{RMS} values, experiences large variations throughout movement sweeps as illustrated in Fig. 8. These values depend on the probability that the shadowing phenomenon occurs when the LOS is obstructed, and on

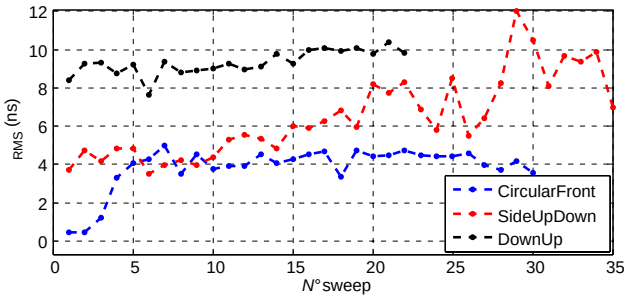

Figure 8. Plot of the τ_{RMS} values for different sweeps in dynamic environment.

the distance between Transmitter and Receiver. Generally, the first sweeps, relating to the case where the arm in starting position, present generally the lowest τ_{RMS} values. The evolution of the channel characteristics along the wrist movement will be exploited to evaluate the performances of the proposed scheme in a dynamic environment. An overview of the conventional UWB-based MultiBand-OFDM (MB-OFDM) and the structure of the proposed technique will be detailed in subsequent section.

3. NEW HIGH-RATE UWB SCHEME: MB-OFDM/OQAM

In the conventional UWB-based Multi Band-OFDM (MB-OFDM) approach [10], the available UWB spectrum (3.1–10.6 GHz) is divided into 14 subbands, each with 528 MHz bandwidth. This configuration was justified previously in many works. The results carried over from [11, 12], where the Degrees Of Freedom (DOF) of the UWB channel were estimated, show that the DOF number N_{DOF} exhibits a saturation behavior beyond a certain bandwidth value BW_C. This being so, why would we use once entirely the bandwidth of 7.5 GHz when it will bring nothing to the diversity and the capacity of the propagation channel? In other words, if we use a bandwidth of $BW > BW_C$, the maximal order of channel diversity will also be reached previously. That is why we opted herein for a multi-band approach that has proven its worth previously. The use of Orthogonal Frequency Division Multiplexing (OFDM) within the MB-OFDM approach is due to very high-data rate, spectral efficiency and immunity towards frequency selectivity.

3.1. UWB-Based MB-OFDM

The physical layer architecture of the MB-OFDM system is similar to that of a conventional OFDM one, except that the carrier frequency changes from one symbol to another according to a Frequency-Hopping Code (FHC). The purpose of the FHC is to interleave the used frequency subband. They are used not only for providing frequency diversity but can also ensure multiple access. The block diagram of the MB-OFDM transmitter is depicted in Fig. 9. Accordingly, the binary stream is first encoded using convolutional coding. The encoded bits are interleaved before being constellated using QPSK mapping. Afterwards, the parallel complex symbols are fed into the Inverse Fast Fourier Transform (IFFT) to

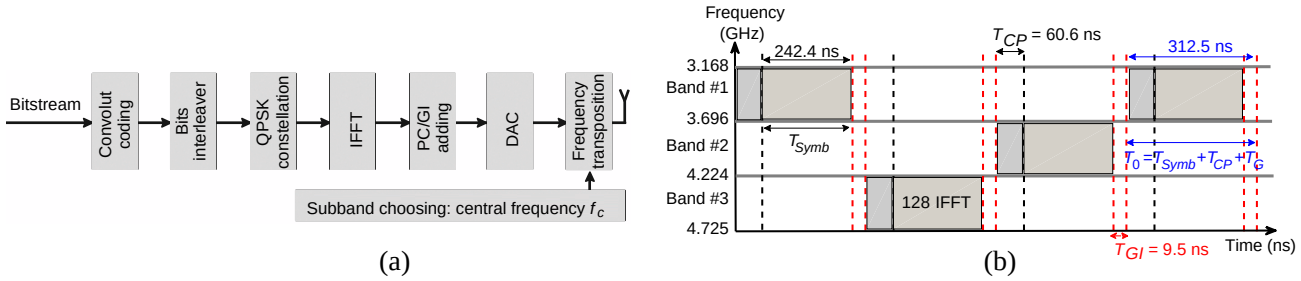

Figure 9. The block diagram of the MB-OFDM transmitter, and the resulted MB-OFDM signal.

generate the baseband OFDM symbol. The total number of subcarriers in each OFDM symbol is 128, of which, there are 100 data subcarriers, 12 pilot subcarriers, 10 guard subcarriers, and the rest are null subcarriers. the resulted symbols are suffixed using a cyclic prefix in the order of 25% of the symbol time $T_{Symb} = 242.4\,\text{ns}$, as well as a guard interval of duration $T_{GI} = 9.5\,\text{ns}$ for providing sufficient time to transceiver to switch from one subband to another. The endpoint is a symbol with a total duration of 312.5 ns, which will be transposed using a frequency subband, depending on the corresponding FH-code. At the MB-OFDM receiver, the signal will be processed in the reverse order.

However, the MB-OFDM transceiver present a few limitations. Indeed, the use of the Cyclic-Prefix involves a partial loss of transmission rate. Moreover, it has been well established that for maintaining the orthogonality between subcarriers in the multicarrier modulation OFDM, only the rectangular prototype function can be used (Balian-Low theorem [13] of the Weyl-Heisenberg families [14]). This rectangular function is yet poorly localized in Time/Frequency domain, which can result in serious Inter-Carriers Interferences (ICI) when Carrier-Frequency Offset (CFO) arises. The introduction of the Offset-QAM (OQAM) as a modulation scheme in the MB-OFDM transceiver scheme seems to be more effective struggle against these limitations. For this reason, a new High-rate Multi Band/Carriers UWB-based scheme will be introduced and described herein.

3.2. Transmitter Structure

Common to the MB-OFDM, each subband contains $N_p = 128$ subcarriers with intercarrier spacing of $\upsilon_0 = 4.125\,\text{MHz}$. The implementation of the 128-tone coefficient vector will be identical to that of MB-OFDM described previously. The MB-OFDM symbol is formed by inserting data block between the 32-samples zero prefix (T_{CP}) and 5-sample guard interval suffix (T_{GI}), making the total symbol length $L = 165$. However, the MB-OFDM/OQAM system has the particularity of transmitting OQAM symboles instead of QPSK. For a given carrier, if the time offset is introduced onto imaginary part of the complex QAM symbol, the real part of the symbol is affected by offset for the adjacent one. Therefore, the real part $a^R_{m,n}$ and the imaginary part $a^I_{m,n}$ of the symbol $a_{m,n}$ are transmitted separately with a symbol duration τ_0 and inter-carrier frequency spacing υ_0, with $\tau_0\upsilon_0 = 1/2$. This time symbol shortening results on the circumventing of the limitations entailed by the Balian-Low theorem [13] for Weyl-Heisenberg [14] families. The difference between the lattices of the conventional MB-OFDM and the MB-OFDM/OQAM are shown in Fig. 10. As can be observed, a complex MB-OFDM symbol (circular sign) is transmitted every period τ_0, while a real symbol (triangular and diamond sign) is transmitted every half period $\tau_0/2$ in the case of MB-OFDM/OQAM.

According to the MB-OFDM/OQAM transmission scheme defined in Fig. 10 and assuming that the number of subcarriers is even valued $N_p = 2M_p$, the expression of the kth continuous-time transmitted

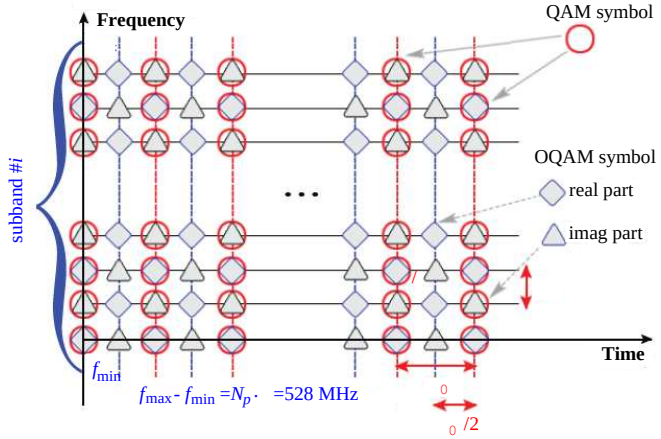

Figure 10. Comparison between time/frequency lattices of the conventional MB-OFDM Vs. MB-OFDM/OQAM.

symbol can be written in the following analytic form:

$$S_k(t) = \sum_{m=0}^{M_P-1} \left[a^{\Sigma}_{2m,n,k} \cdot e^{2j\pi\left(f_{k_{\min}}+2m\upsilon_0\right)t} + a^{\Sigma}_{2m+1,n,k} \cdot e^{2j\pi\left(f_{k_{\min}}+(2m+1)\upsilon_0\right)t} \right] \tag{1}$$

where

$$\begin{cases} a^{\Sigma}_{2m,n,k} = \left(a^{R}_{2m,n,k} g(t-nT_0) + j a^{I}_{2m,n,k} g\left(t-nT_0-T_0/2\right) \right) \\ a^{\Sigma}_{2m+1,n,k} = \left(a^{R}_{2m+1,n,k} g(t-nT_0-T_0/2) + j a^{I}_{2m+1,n,k} g(t-nT_0) \right) \end{cases} \tag{2}$$

are the offset version of the symbol $a_{m=0\ldots N_p-1,n,k\in\mathbf{Z}}$, which represents the nth symbol conveyed on the mth subcarrier (N_p available carriers), across the kth frequency band. The function $g_{m,n,k}(t)$ denotes the Time-Frequency translation of the prototype function $g(t)$ that forms the synthesis basis. The pulses g are designed in such a way as to maintain the orthogonality in real field:

$$\Re\{< g_{m,n,k} | g_{p,q,k'} >\} = \Re\left\{ \int g_{m,n,k}(t) g^*_{p,q,k'}(t) dt \right\} = \delta_{m,p}\delta_{n,q} \tag{3}$$

where $\delta_{i,j}$ is the Kronecker operator (i.e., $\delta_{i,j} = 1$ if $i = j$ and $= 0$ otherwise). For the sake of simplification, we denote:

$$\begin{aligned} a_{2m,2n,k} &= a^{R}_{2m,n,k}; \quad a_{2m,2n+1,k} = a^{I}_{2m,n,k} \\ a_{2m+1,2n+1,k} &= a^{R}_{2m+1,n,k}; \quad a_{2m+1,2n,k} = a^{I}_{2m+1,n,k} \\ g_{2m,2n,k}(t) &= g(t-nT_0) e^{2j\pi\left(f_{k_{\min}}+2m\upsilon_0\right)t} \\ g_{2m,2n+1,k}(t) &= j g(t-nT_0-T_0/2) e^{2j\pi\left(f_{k_{\min}}+2m\upsilon_0\right)t} \\ g_{2m+1,2n+1,k}(t) &= g(t-nT_0-T_0/2) e^{2j\pi\left(f_{k_{\min}}+(2m+1)\upsilon_0\right)t} \\ g_{2m+1,2n,k}(t) &= j g(t-nT_0) e^{2j\pi\left(f_{k_{\min}}+(2m+1)\upsilon_0\right)t} \end{aligned} \tag{4}$$

The expression of the kth symbol becomes:

$$S_k(t) = \sum_{m=0}^{2M_P-1} a_{m,n,k} g_{m,n,k}(t) \tag{5}$$

Symbol $S_k(t)$ can be seen as an expansion of the coefficients $a_{m,n,k}$ over the basis functions. The MB-OFDM/OQAM symbol includes a frequency index noted k, to determine for each symbol which frequency carrier must be used by referring to the FH-code aforementioned. Therefore, the $f_{k_{\min}} = f_{k_c} - \Delta f/2$ designates the minimum frequency of the kth subband, which equals 0 when this symbol is expressed in baseband notation, and f_{k_c} is the central frequency of this kth subband. For conventional MB-OFDM scheme, the prototype function is the rectangular function of length $T_{CP}+T_{Sym}$, known for being poorly localized in frequency domain. For the MB-OFDM/OQAM system, the prototype function is given as:

$$g_{m,n}(t) = e^{j(m+n)\pi/2} e^{j2\pi m\upsilon_0 t} g(t-n\tau_0); \quad \tau_0\upsilon_0 = 1/2 \tag{6}$$

the term $\varphi_{m,n} = e^{j(m+n)\pi/2}$ is introduced for dephasing the symbol $a_{m,n}$. Contrary to MB-OFDM, The prototype function $g(t)$ can be chosen among several pulse shape functions as long as being even for ensuring the orthogonality between different sub-lattices [15]. The continuous-time baseband transmitted MB-OFDM/OQAM signal can be expressed as:

$$S(t) = \sum_{n=0}^{+\infty} S_k(t) = \sum_{n=0}^{+\infty} \sum_{m=0}^{2M_P-1} a_{m,n,k} g_{m,n,k}(t) \tag{7}$$

As pointed out, the expression of the MB-OFDM/OQAM signal does not feature the frequency band index k, since the link between time indies n and k ($f : n \mapsto k$) is surjective: Knowing index n

of time interval in which symbol S_k is transmitted, we can reveal index k of the kth subband by taking into account the FH-code of transmission.

The transmission system consists of various blocks as shown in Fig. 11. As for the standard ECMA-368 [16] defining the UWB radio platform, this system begins with a Bernoulli binary generator, which generates a frame-based random binary flow following the Bernoulli distribution, followed by channel encoding using convolutional code and puncturing for reaching different code rates. The Base code rate of 1/3 convolutional encoder with constraint length $K = 7$ and generator polynomial of $g_0 = [133]$, $g_1 = [165]$ and $g_2 = [171]$ is adopted. Other code rates can be then achieved using the puncturing method, while decoding is performed using the Viterbi algorithm with hard decision. After this, a bit Interleaving process is used to deliver robustness against burst error and narrow-band interferences. Then, the interleaved message is constellated using QPSK before a real mapping and symbol dephasing (offset $= T/2$) between real and imaginary part according to OQAM scheme. Frequency diversity consists on the use of a frequency hopping technique in which the frequency band is hopped using a FH-code (also known as Time-Frequency-Code) known by both transmitter and receiver. This TF-code

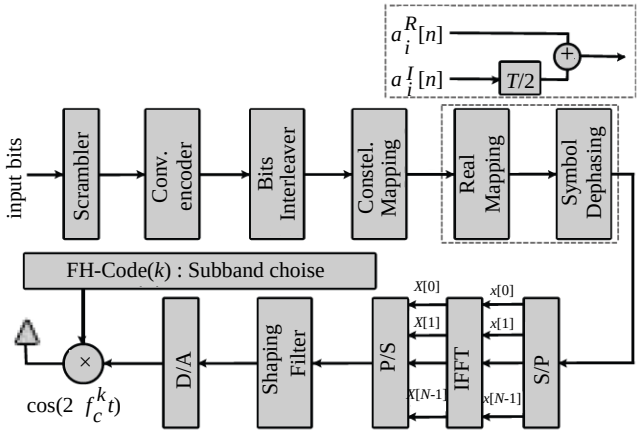

Figure 11. MB-OFDM/OQAM transmitter blocks.

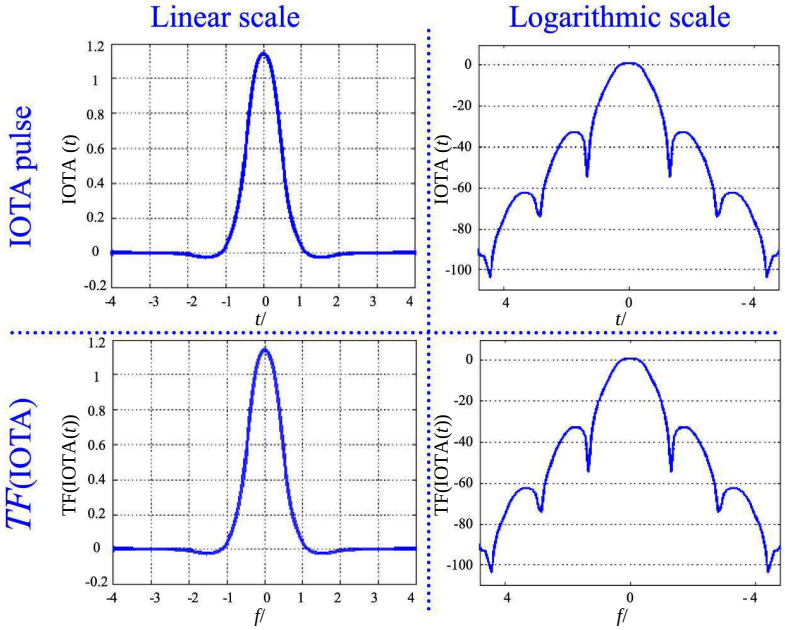

Figure 12. Representation of the IOTA pulse and its Fourier transform.

serves to determine the kth frequency carrier f_c^k, in view of transposing the carrier frequency of the generated signal to f_c^k.

As mentioned in [13], the shaping pulse $g(t)$ must be real-valued and symmetrical, and may differ from the rectangular function which can be used as a benchmark for comparison. Similarly, the Isotropic Orthogonal Transform Algorithm (IOTA) pulse shows a good Time/Frequency Localization (TFL) according to the maximal value of Heisenberg parameter. This pulse can be derived by orthogonalizing the Gaussian pulse in time and frequency [13]. Such pulse are called root-Nyquist self-transform pulses and are known to have a Fourier transform identical to the pulse itself as shown in Fig. 12.

3.3. MB-OFDM/OQAM Receiver Structure

The block diagram of the MB-OFDM/OQAM receiver considered herein is depicted in Fig. 13. At the reception, each received signal $r(t)$ will be divided into a sequence of signals $r_k(t)$, that in turn will be expressed in baseband notation using the kth FH-code. The signal $r(t)$ is filtered by a channel impulse response denoted $h(t,\tau)$, also in presence of an additive noise denoted by $\eta(t)$. The baseband notation of the received signal can be then written as follows:

$$r(t) = (h * s)(t) + \eta(t) \tag{8}$$

where $*$ is the convolution operator. Denoting by r_{NF} the noise-free signal from the channel output, it can be represented by:

$$r_{NF}(t) = \sum_{n=0}^{\infty} \sum_{m=0}^{2M_P-1} a_{m,n,k} \int_0^{\Delta} h(t,\tau) g_{m,n,k}(t-\tau) d\tau \tag{9}$$

According to Equation (6), this expression can be expanded as follows:

$$r_{NF}(t) = \sum_{n=0}^{\infty} \sum_{m=0}^{2M_P-1} a_{m,n,k} e^{j\varphi_{m,n}} e^{2j\pi m\upsilon_0 t} \times \int_0^{\Delta} h(t,\tau) g(t-\tau-n\tau_0) e^{-2j\pi m\upsilon_0 \tau} d\tau \tag{10}$$

If we consider T_g the length of the prototype filter with $T_g = kT_0$, where k is generally taken as equal to 4. The value of T_g must be taken in such a way as to assume that the channel is flat at each subcarrier. It means that $\frac{1}{T_g}$ is less than the coherence bandwidth of the channel $B_c \approx \frac{1}{2\Delta}$. That said, the prototype function has low variations over the interval $[0,\Delta]$: for $\tau \in [0,\Delta]$, $g(t-\tau-n\tau_0) \approx g(t-n\tau_0)$. Then we have:

$$r_{NF}(t) = \sum_{n=0}^{\infty} \sum_{m=0}^{2M_P-1} a_{m,n,k} g_{m,n,k}(t) H_{m,n,k}(t) \tag{11}$$

where $H_{m,n,k}(t)$ is the frequency channel response for the mth subcarrier for the nth symbol over the kth frequency band. Specifically, this can be expressed by:

$$H_{m,n,k}(t) = \int_0^{\Delta} h(t,\tau) e^{-2j\pi m\upsilon_0 \tau} d\tau \tag{12}$$

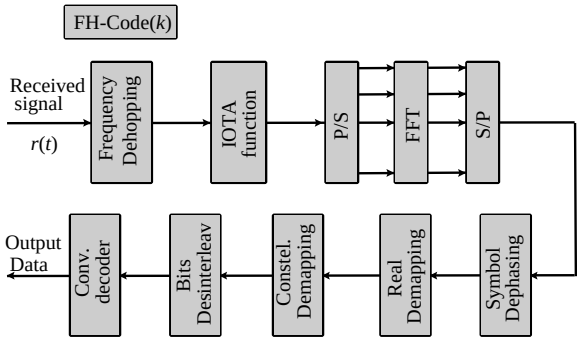

Figure 13. The proposed MB-OFDM/OQAM receiver.

We assume that the channel is constant for a symbol over a given subband $H_{m,n,k}(t) = H_{m,n+1,k}(t)$. Therefore, when the used subband is changed, this involves the need for re-estimate new channel response parameters. Being so, the major proportion of the prototype function must be located in a reduced time interval. In what follows we will present the process of demodulation and equalization.

3.4. Demodulation and Equalization

The process of the demodulation and equalization is done by extracting simultaneously the different symbols sent over different subbands, before expressing them in baseband notation through the frequency dehopping process. The demodulation operation of the received noise-free signal in the position (m_0, n_0, k_0) involve the use of the prototype function $g_{m_0,\,n_0,\,k_0}$ as follows:

$$r'_{m_0,n_0,k_0} = \langle r | g_{m_0,n_0,k_0} \rangle \tag{13}$$

By expanding this equation using the expression of the received noise-free signal r_{NF} and the prototype function g_{m_0,n_0,k_0} we obtain:

$$\begin{aligned} r'_{m_0,n_0,k_0} &= \langle r_{NF} | g_{m_0,n_0,k_0} \rangle \\ &= H_{m_0,n_0,k_0} a_{m_0,n_0,k_0} + j \sum_{(p,q)\neq(0,0)} a_{m_0+p,n_0+q,k_0} H_{m_0+p,n_0+q,k_0} g_{(m,n),(p,q)} \end{aligned} \tag{14}$$

which means that even when the additive noise is absent, some Inter-Carrier (Inter-Symbols) interferences will be carried out. These intrinsic interferences are expressed by introducing the term $g_{(m,n),(p,q)}$ where:

$$\sum_t g_{m,n}(t) g^a st_{p,q}(t) = j g_{(m,n),(p,q)} \tag{15}$$

However, the choice of pulses g that are well localized in time and frequency domain is of key importance, since it can alleviate the interferences in a point (m_0, n_0, k_0) from his neighborhood Ω_{m_0,n_0,k_0}. In the ideal channel case, the channel response can be considered as Dirac peaks ($H_{m_0,n_0,k_0} = 1$). Then the expression of the received signal of Eq. (14) can be rewritten as:

$$r'_{m_0,n_0,k_0} = a_{m_0,n_0,k_0} + \underbrace{j \sum_{(p,q)\neq(0,0)} a_{m_0+p,n_0+q,k_0} g_{(m,n),(p,q)}}_{Imaginary\ term} \tag{16}$$

The estimation of the symbols a_{m_0,n_0,k_0} can be done by using the real operator of the received signal:

$$\hat{a}_{m_0,n_0,k_0} = \Re\left\{ r'_{m_0,n_0,k_0} \right\} = a_{m_0,n_0,k_0} \tag{17}$$

However, in the usual case the channel is not ideal, hence the need for a one-tap equalizer. For example, the equalized signal using Zero-Forcing equalizer can be written as:

$$\frac{r'_{m_0,n_0,k_0}}{H_{m_0,n_0,k_0}} = a_{m_0,n_0,k_0} + \underbrace{j \sum_{(p,q)\neq(0,0)} a_{m_0+p,n_0+q,k_0} g_{(m,n),(p,q)} \frac{H_{m_0+p,n_0+q,k_0}}{H_{m_0,n_0,k_0}}}_{Interference\ term\ I_{m_0,n_0,k_0}} \tag{18}$$

where the interference term I_{m_0,n_0,k_0} is complex-valued. The estimation of the received symbols a_{m_0,n_0,k_0} can be retrieved as:

$$\begin{aligned} \widehat{a}_{m_0,n_0,k_0} &= \Re\left\{ \frac{r'_{m_0,n_0,k_0}}{H_{m_0,n_0,k_0}} \right\} \\ &= a_{m_0,n_0,k_0} + \Re\{I_{m_0,n_0,k_0}\} \\ &= a_{m_0,n_0,k_0} + \sum_{(p,q)\neq(0,0)} a_{m_0+p,n_0+q,k_0} \times g_{(m,n),(p,q)} \Im\left\{ \frac{H_{m_0+p,n_0+q,k_0}}{H_{m_0,n_0,k_0}} \right\} \end{aligned}$$

The interference term indicates the presence of Inter-Symbols interferences between successive real symbols, so it is difficult to retrieve an accurate estimate of the symbols a_{m_0,n_0,k_0}, expect where the interference term is null $I_{m_0,n_0,k_0} = 0$. These ISI come primarily from the neighborhood $\Omega^{\varrho_1,\varrho_2}_{m_0,n_0,k_0} = \{a_{p,q,k'} | p = m_0 + \varrho_1; q = m_0 + \varrho_2\}$, which represents the adjacent positions to the mth carrier of the nth symbol over the kth subband where ϱ_1 and ϱ_2 are the frequency and time neighborhood depth. The strongest interferences come from the adjacent neighborhood $\Omega^{1,1}_{m_0,n_0,k_0}$, while the power of these ISI decreases as the neighboring depth increases. The interference term generated by the neighborhood $\Omega^{\varrho_1,\varrho_2}_{m_0,n_0,k_0}$ is not considered as affecting the current symbol a_{m_0,n_0,k_0} if the following condition is melt:

$$\Omega^{\varrho_1,\varrho_2}_{m_0,n_0,k_0} = \{a_{p,q,k'} \mid H_{m_0,n_0,k_0} \approx H_{m_0+\varrho_1,n_0+\varrho_2,k_0}\} \tag{19}$$

That said, ϱ_1 and ϱ_2 can be selected by taking into account the values of the coherence bandwidth B_C and the time of coherence T_C: The coherence time (coherence bandwidth) indicates the time (frequency) interval during which the channel is approximately constant and then, when increasing T_C (resp. BC) the value of ϱ_2 (ϱ_1) will also increase.

The restriction of these interferences into a limited zone is amongst the main reasons for choosing a shaping function well-localized in time and frequency domains. A major benefit of using the IOTA function as pulse shaping is that its energy is isotropically spread towards time and frequency domain. The greater the spread of the shaping function energy is, the larger a neighboring symbol filtered by the prototype filter can interfere. Indeed, these interferences become close to zero with increasing the values of the depth ϱ_1 and ϱ_2. In practice, for well-localized prototype functions these interferences can be neglected and thereby, an accurate estimation for the emitted symbols can be performed if we are to know the real channel coefficients H_{m_0,n_0,k_0}. For this reason, the pilot symbols are transmitted at a position (m_0, n_0, k_0) despite being known by the receiver to derive directly the values of H_{m_0,n_0,k_0}. Next we will introduce the channel estimation algorithm adopted herein for assessing the transmission scheme.

4. PERFORMANCE EVALUATION

In order to evaluate the performance of the proposed technique for WBANs physical layer, several simulations have been done for implementing the conventional MB-OFDM and the proposed MB-OFDM/OQAM for realistic WBANs scenarios. These experiments were implemented in mandatory mode. Only the three first subbands were considered, with a convolutional code (rate = 1/3) and a QPSK constellation for MB-OFDM, which corresponds to a transmission rate of 53.5 Mbits/S. As to MB-OFDM/OQAM, the gain resulting from eliminating the cyclic prefix was around 33% (77.1 Mbits/S).

First experiments are implementing both techniques (MB-OFDM & MB-OFDM/OQAM) to evaluate the transmission quality, in terms of Binary Error Rate (BER) as a function of the Signal/Noise Ratio (SNR), where the receiver is considered static vis-vis the transmitter. For personal and acoustic applications, the adopted threshold for system outage is 0.1%, corresponding to a BER of 10^{-3} to be tolerable for such applications. The BER values as a function of the SNR (dB) is expressed in Fig. 14. As can be seen, the use of OQAM in the MB-OFDM configuration presents best performances in terms of transmission BER. For high noisy environments ($RSB < -5\,\text{dB}$), both techniques have the same performances, whereas they are sharply distant since $RSB = -5\,\text{dB}$ (0 dB for *Rx-On-Chest*). The MB-OFDM/OQAM gain can be as high as 5 dB. This amelioration was observed even when the rectangular waveform was used, for both MB-OFDM and MB-OFDM/OQAM. The use of the shaping filter presents a tradeoff between system performance and complexity. Increasing the complexity of the system, the performance will be clearly enhanced. Fig. 15 gives an example of performance amelioration when introducing the IOTA shaping filter for the MB-OFDM/OQAM system. Despite increasing implementation complexity, the resulted performance has been upped considerably.

The receiver sensitivity represents an important parameter for assessing a proposed WBANs physical layer system. Indeed, it means the minimum signal power level for reaching a specific system gain. For WBANs, the receiver sensitivity translates the minimum receiver power in order to reach a BER value of $TEB < 1e^{-3}$ for a given SNR level. The expression of the receiver sensitivity (dB) can be given by:

$$S\,(\text{dBm}) = -174 + NF + 10\log(BW) + 10\log(S/N) \tag{20}$$

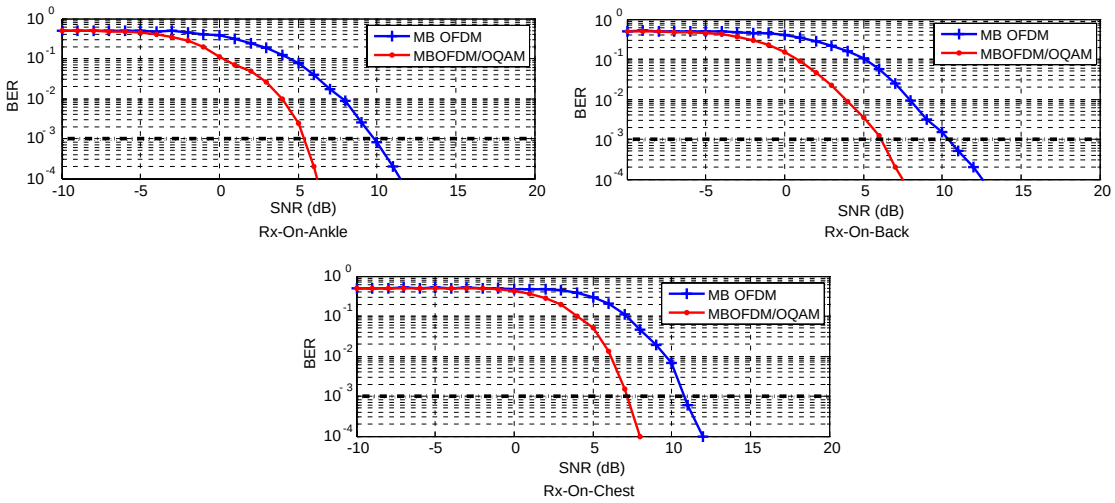

Figure 14. Comparison of the performances of the MB-OFDM vs. MB-OFDM/OQAM in static configuration, *Tx-on-waist*.

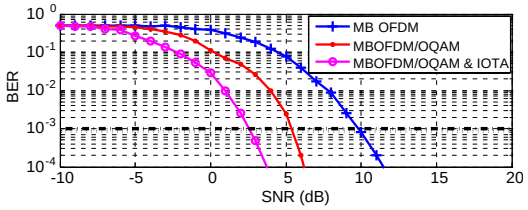

Figure 15. MBOFDM/OQAM performances when introducing IOTA shaping filter.

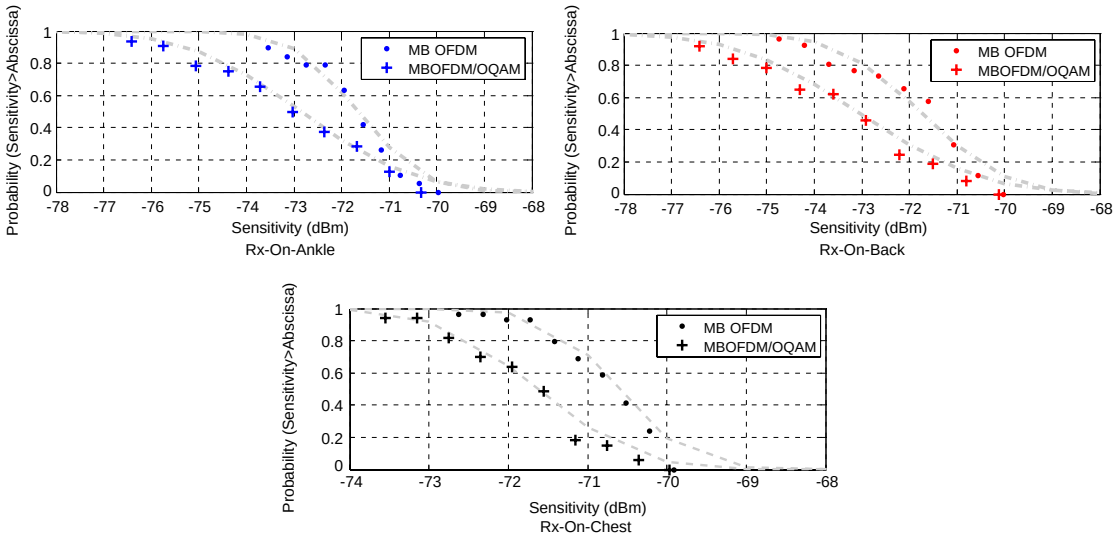

Figure 16. Distribution of estimated receiver sensitivity for both MB-OFDM and MBOFDM/OQAM, for different configurations.

where $S\,(\mathrm{dBm})$ is the receiver sensitivity, NF the Noise Figure, $BW\,(\mathrm{Hz})$ the available bandwidth, and S/N the minimum value of SNR for reaching a specific value of BER ($1e^{-3}$). For example, when $NF = 4\,\mathrm{dB}$, Fig. 16 illustrates the calculated receiver sensitivity values as well as for MB-OFDM and the MB-OFDM/OQAM. We can observe that the Offset-QAM introduced in the proposed technique

can reduce the receiver sensitivity for different configurations, where Rx is considered static compared to Tx. This parameter has an impact on the communication range and on the antenna size. Indeed, every antenna has a specific value named aperture, serving to define the amount of power which can be collected. Therefore, for maximizing the capacity of collected energy, the aperture value must be incremented, which is the same as increasing the antenna dimension. This represents a major challenge for designing systems dedicated to WBANs.

However, as aforementioned, the corps disposition is not always static. This is why we will try to evaluate the system performance when the arm is in motion, as described in Fig. 6. The BER values will be calculated for different arm motion sweeps. Fig. 17 shows plots of the BER values as a function of the sweep index, for different antenna configurations where $SNR = 10\,\text{dB}$. We can observe that the amelioration can be provided by the proposed technique. For example, when the wrist moves circularly in front of the body, 24/30 sweeps are acceptable ($TEB < 1E-3$) for the MB-OFDM/OQAM, while just 18/30 are retained for the MB-OFDM. Some observation was found for the Side-Up-Down motion, where the acceptance rate for the proposed technique was about 10/30, while only 1/30 was observed for the MB-OFDM. This configuration is the worst one, since the Line Of Sight is always obstructed by the human body.

In all cases, the proposed MB-OFDM/OQAM exhibits much better results than MB-OFDM and increases the transmission rate (about +33%). However, the complexity of implementation must be investigated. For this reason, the number of operations needed for modulating the signal will be calculated in both configurations. When a data block of N symbols must be processed, a Fourier transform of N entries must be realized. This necessitates a total of $N/2 \log_2 N$ complex multiplications, equivalent to $2N \log_2 N$ real operations. Therefore, the implementation complexity of the MB-OFDM system is about $N_B(2N \log_2 N)$, where N_B is the number of used subbands (Length of TF-code).

For MB-OFDM/OQAM, the modulator has the same complexity as the demodulator. As a consequence, a Fourier transform of dimension N is done every half-time of symbol. The system complexity is then equal to $N_B(4N \log_2 N)$. When using the shaping filter (length L_g), the complexity is increased by $4L_gN$ real multiplications, which results in a total complexity of $N_B(4N \log_2 N + 4L_g)$.

This will result in an increase on the implementation complexity as a price of performance improvement. However, many works present interesting scheme for decreasing the complexity of the OQAM modulation. For example in [17], new implementations for OFDM based on offset QAM (OFDM-OQAM) were derived. This configuration nearly halves the number of arithmetic operations required for every symbol period, by exploiting the symmetries in the transmitted sequences. As a consequence,

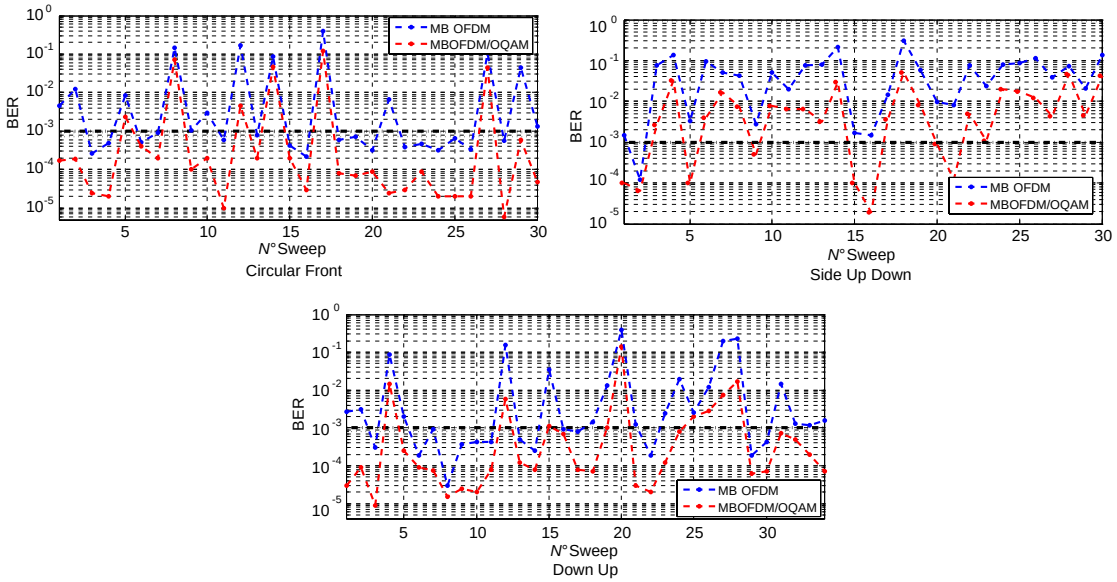

Figure 17. Binary error rate for different arm motion sweeps.

the MB-OFDM/OQAM complexity will become equal to $N_B(2\log_2 N + 4L_g + 4 - 8/N)$, which is close to the value found for the MB-OFDM, especially when no shaping filter is used.

5. CONCLUSION

In this paper, an investigation about the characteristics of the UWB in presence of human body is carried out. The propagation channel measurements are performed in order to study the deterministic characteristics of the radio channel in the presence of human body, including the Path-Loss and excess delay parameters. Afterwards, a new physical layer scheme for high-rate wireless body area networks, named MB-OFDM/OQAM is presented and evaluated relatively to the conventional MB-OFDM. In addition to the increase of data-rate transmission, the proposed MB-OFDM/OQAM can achieve higher spectral and power efficiency than conventional MB-OFDM system, together with reducing the factor form of the antennas, which represents significant challenges for Wireless Body Area Networks.

ACKNOWLEDGMENT

Special thanks for Mr. Qammer Abbasi from Mary-Queen London University for his cooperativeness and valuable help.

REFERENCES

1. Hämäläinen, M., P. Pirinen, Z. Shelby, and J. Iinatti, "Wireless applications in healthcare and welfare," *Advances in Mobile and Wireless Communications: Views of the 16th IST Mobile and Wireless Communication Summit, Lecture Notes in Electrical Engineering*, Vol. 16, 351–364, I. Frigyes, J. Bito, P. Bakki, Eds., 2008.
2. Pan, J., "Medical applications of ultra-wideband (UWB)," Apr. 2008, Available Online: http://www1.cse.wustl.edu/ jain/cse574-08/ftp/uwb/index.html.
3. Gyselickx, B., C. Van Hoof, J. Ryckaert, et al., "Human ++: Autonomous wireless sensors for body area networks," *Proc. IEEE Custom Integr. Circuits Conf.*, 13–19, Sep. 2005.
4. Yuce, M. R., et al., "A MICS band wireless body sensor network," *IEEE Wireless Communications and Networking Conference*, 2473–2478, 2007.
5. Yu, B. and L. Yang, "ECG monitoring over Bluetooth: Data compression and transmission," *IEEE Wireless Communications and Networking Conference*, 1–5, 2010.
6. Keong, H. C. and M. R. Yuce, "Low data rate ultra wideband ECG monitoring system," *IEEE Engineering in Medicine and Biology Society Conference (IEEE EMBC08)*, 3413–3416, Aug. 2008.
7. Miranda, H., V. Gilja, C. A. Chestek, K. V. Shenoy, and T. H. Meng, "HermesD: A high-rate long-range wireless transmission system for simultaneous multichannel neural recording applications," *IEEE Transactions on Biomedical Circuits and Systems*, Vol. 4, No. 3, 181–191, Jun. 2010.
8. Anliker, U., et al., "AMON: A wearable multiparameter medical monitoring and alert system," *IEEE Transactions on Information Technology in Biomedicine*, Vol. 8, 415–427, 2004.
9. Di Bari, R., Q. H. Abbasi, A. Alomainy, and Y. Hao, "An advanced UWB channel model for body-centric wireless networks," *Progress In Electromagnetics Research*, Vol. 136, 79–99, 2013.
10. Batra, A., J. Balakrishnan, G. R. Aiello, J. R. Foerster, and A. Dabak, "Design of a multiband OFDM system for realistic UWB channel environments," *IEEE Transactions on Microwave Theory and Techniques*, Vol. 52, No. 9, 2123–2138, 2004.
11. Mohammadi, Z., R. Saadane, and D. Aboutajdine, "Improving the estimation of the degrees of freedom for UWB channel using wavelet-based denoising," *European Journal of Scientific Research*, Vol. 79, No. 4, 577–591, Jul. 2012.
12. Saadane, R., A. Menouni, R. Knopp, and D. Aboutajdine, "Empirical eigenanalysis of indoor UWB propagation channels," *IEEE Global Telecommunications Conference, GLOBECOM' 04*, Vol. 5, 3215–3219, 2004.

13. Le Floch, B., M. Alard, and C. Berrou, "Coded orthogonal frequency division multiplex [TV broadcasting]," *Proceedings of the IEEE*, Vol. 83, No. 6, 982–996, 1995.
14. Daubechies, I., "The wavelet transform, time-frequency localization and signal analysis," *IEEE Transactions on Information Theory*, Vol. 36, No. 5, 961–1005, 1990.
15. Du, J. and S. Signell, "Time frequency localization of pulse shaping filters in OFDM/OQAM systems," *6th International Conference on Information, Communications & Signal Processing*, Singapore, Dec. 2007.
16. Standard ECMA-368, *High Rate Ultra Wideband PHY and MAC Standard*, 3rd Edition, ECMA International, Dec. 2008.
17. Vangelista, L. and N. Laurenti, "Efficient implementations and alternative architectures for OFDM-OQAM systems," *IEEE Transactions on Communications*, Vol. 49, No. 4, 664–675, Apr. 2001.